

Universal Centimeter-Scale van der Waals Epitaxy of Ultrathin Single-Crystalline Ferrites Films

Yanchang Zhou, Ruiqing Cheng,* Shuyang Yuan, Xiaoqiang Feng, Yushan Zhu, Sheng Jiang, Hao Wang, Lei Yin, Yao Wen, Wei Liu,* and Jun He*

2D magnetic materials offer significant potential for advanced spintronics, but their practical implementation is hindered by fundamental limitations such as low Curie temperatures and the current inability to achieve scalable, large-area synthesis. Herein, a significant breakthrough in the centimeter-scale epitaxial growth of ultrathin single-crystalline magnetic ferrite films, including cobalt ferrite, manganese ferrite, and nickel ferrite is reported. By leveraging symmetry-matching-induced energy splitting between antiparallel orientations and developing a precisely engineered nucleation timing strategy to amplify synergistic coupling, unidirectional epitaxial growth with seamless domain coalescence is achieved. Comprehensive macro- and micro-characterizations confirmed the single-crystalline nature and high quality. Vibrating sample magnetometry measurements reveal robust ferrimagnetism persisting up to 730 K, while magneto-optical Kerr effect microscopy visualized sharp uniform single-domain switching behavior. Interestingly, two potential strategies have been explored for heteroepitaxial integration of CFO thin films with engineered substrates. This work establishes a scalable and viable synthesis route for 2D magnetic oxides, marking a pivotal step toward their practical deployment in high-performance spintronic and quantum devices.

past decade, seminal discoveries such as intrinsic magnetism in atomically thin CrI_3 ,^[4–6] CrBr_3 ,^[7] Fe_3GaTe_2 ,^[8–10] $\text{Cr}_2\text{Ge}_2\text{Te}_6$ ^[11] and FeTe ^[12] have ignited intense research efforts to explore 2D magnetism. However, despite these breakthroughs, significant challenges persist in synthesizing large-area, high-quality single-crystalline 2D magnetic films with robust magnetic properties at room temperature. Most reported 2D magnets suffer from low Curie temperatures, poor ambient stability, or limited lateral dimensions, severely hindering their practical applicability. In the meantime, the development of 2D magnetic oxides (the definition of 2D magnetic oxides is discussed in Note S1, Supporting Information), particularly spinel ferrites with excellent chemical stability^[13] like CoFe_2O_4 (CFO), MnFe_2O_4 (MFO) and NiFe_2O_4 (NFO), has gained momentum due to their high chemical stability, tunable magnetic anisotropy, and room-temperature magnetism.^[14] Although Cheng et al. have realized the epitaxial of

1. Introduction

The emergence of 2D magnetic materials has revolutionized the landscape of condensed matter physics and materials science, offering unprecedented opportunities for next-generation spintronic^[1] and magneto-electronic devices.^[2] Unlike their bulk counterparts, 2D magnetic systems exhibit unique thickness-dependent magnetic ordering, quantum confinement effects, and enhanced interfacial coupling, making them ideal candidates for miniaturized and energy-efficient technologies.^[3] Over the

CFO with atomic-thickness,^[15] achieving macroscopic-area growth remains an unresolved challenge. A paradigm shift in synthetic methodology and a rethinking of epitaxial mechanisms are extremely needed.

Parallel to the pursuit of 2D magnetism, the field of van der Waals (vdW) epitaxy has witnessed remarkable progress in enabling the synthesis of diverse 2D materials on heterogeneous substrates.^[16–20] Traditional epitaxial growth relies on strict lattice matching between the substrate and deposited material to minimize interfacial strain, a requirement that severely limits material compatibility and scalability.^[21,22] In contrast, vdW epitaxy leverages weak interfacial interactions—arising from passivated substrate surfaces or layered structures—to decouple the overlayer from the substrate's lattice constraints.^[23] This paradigm shift has facilitated the growth of transition metal dichalcogenides (TMDCs)^[24] and hexagonal boron nitride (hBN).^[25] However, extending this approach to complex oxides like CFO introduces formidable challenges. Previous attempts to synthesize CFO films have predominantly yielded polycrystalline or multidomain structures,^[26] underscoring the need for a systematic framework to address these limitations.

In this study, we engage with the above challenges by introducing a modified chemical vapor deposition (CVD) approach to

Y. Zhou, R. Cheng, S. Yuan, X. Feng, Y. Zhu, S. Jiang, H. Wang, L. Yin, Y. Wen, W. Liu, J. He
 School of Physics and Technology
 Wuhan University
 Wuhan 430072, China
 E-mail: chengrq@whu.edu.cn; wliu@whu.edu.cn; He-jun@whu.edu.cn
 J. He
 Wuhan Institute of Quantum Technology
 Wuhan 430206, China

The ORCID identification number(s) for the author(s) of this article can be found under <https://doi.org/10.1002/adma.202509037>

DOI: 10.1002/adma.202509037

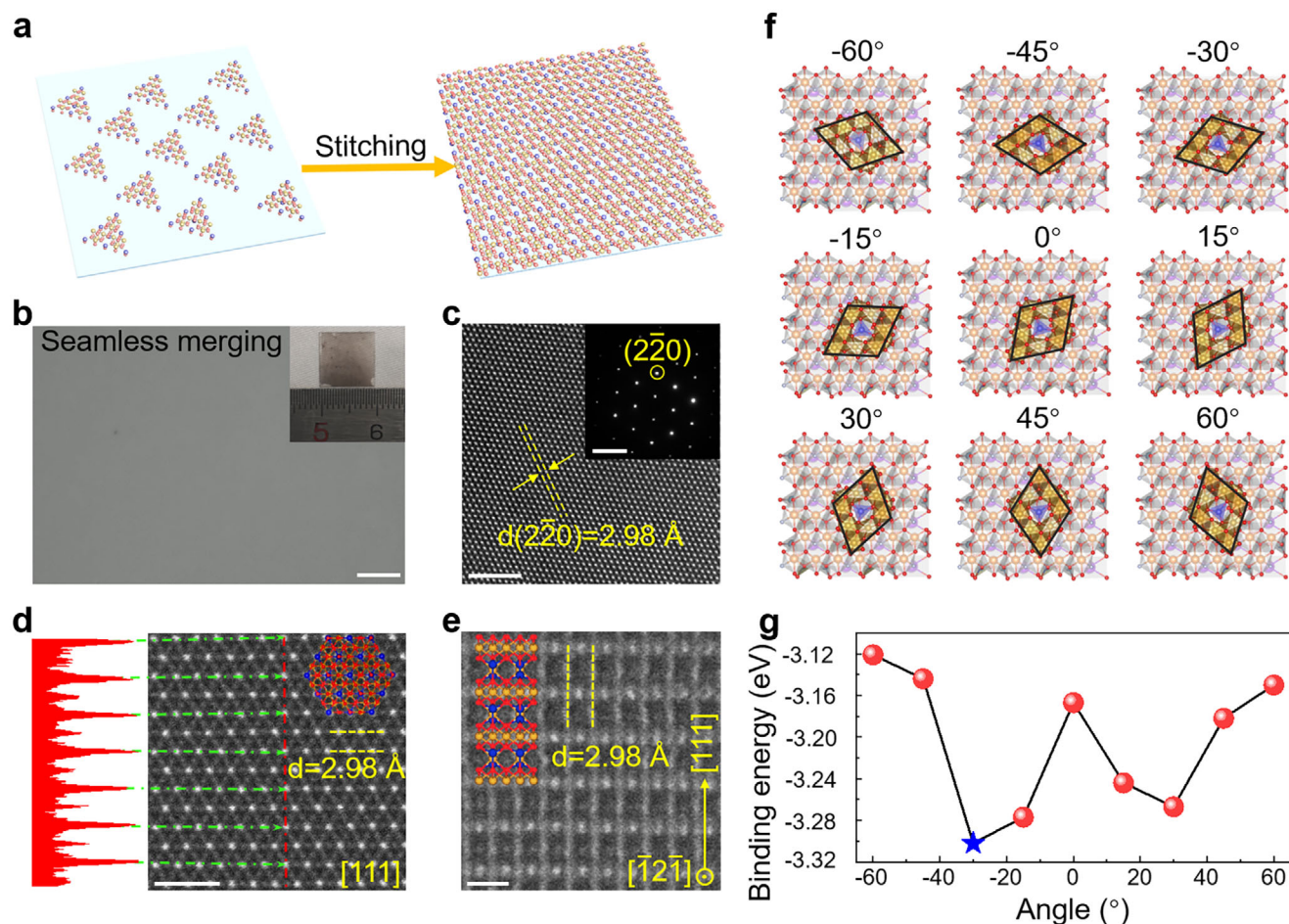


Figure 1. Centimeter-scale synthesis of single-crystalline CFO films by van der Waals epitaxy. a) Schematic illustration of a numbers of unidirectional domains seamlessly merging into a single-crystalline film. b) OM image of CFO (111) film on mica substrate with high visual uniformity. Scale bar: 20 μm. Inset: Photography of CVD-synthesized centimeter-scale CFO film on mica substrate. c) HRTEM image of a transferred CFO film. The lattice spacing is measured to be 2.98 Å, corresponding to its (220) planes. Scale bar: 2 nm. Inset: SAED pattern from the same sample. Scale bar: 5 nm⁻¹. d) Plan-view STEM image of CFO film with the intensity profile taken along the red dash-dot line. Scale bar: 1 nm. e) Cross-sectional STEM image of CFO film. Scale bar: 0.5 nm. f) The structures of CFO (111) domains on fluorophlogopite mica (001) with angles from -60° to 60°, respectively. g) Binding energy of CFO (111) domains on fluorophlogopite mica (001) as a function of angle.

achieve centimeter-scale single-crystalline spinel ferrites films, including CFO, MFO, and NFO. We demonstrate that symmetry matching enables deterministic unidirectional alignment of CFO nuclei, while a considerate nucleation timing ensures cooperative auxiliary amplification. Structural and magnetic characterizations confirm the exceptional crystalline quality, stoichiometric precision, and high-Curie temperature magnetism of the synthesized CFO films, positioning them as promising candidates for industrial-scale spintronic applications. Furthermore, we explore two potential pathways for integrating CFO with engineered substrates, addressing a critical bottleneck in CMOS-compatible device fabrication. This work not only advances the synthesis of 2D magnetic oxides but also establishes a universal framework for vdW epitaxy of complex materials, bridging the gap between 2D magnetic materials and scalable manufacturing.

2. Results and Discussion

Here we demonstrate centimeter-scale CVD growth of ultra-thin single-crystalline CFO films via a strategy employing unidirectional seamless stitching, as conceptually illustrated in Figure 1a. Uniform single-crystalline CFO epitaxial films on 1×1 cm² fluorophlogopite mica substrates were achieved through deliberate modulation of reaction dynamics governed by modulation of the carrier gas (Ar) flow. The corresponding CVD schematic setup is displayed in Figure S1 (Supporting Information) (detailed growth parameters are available in the Experimental Section). It is worth noting that a mixed chloride system comprising FeCl₃ and NaCl was employed to significantly reduce the precursor melting point,^[27] thereby ensuring complete precursor liquefaction and generating sufficient metal precursor vapor pressure. This optimized precursor delivery system enables

large-scale nucleation and uniform epitaxial growth of CFO on mica substrates. Figure 1b presents the optical micrograph (OM) of the centimeter-scale CFO film on mica, revealing well visual uniformity. The corresponding digital photograph inset further confirms the macroscopic uniformity of the entire film. To exclude interference from particle deposition on the backside of the mica substrate, we present a photograph of the CFO film on a polished and cleaned SiO₂/Si in Figure S2 (Supporting Information), reflecting the great uniformity and quality of the films. This represents, to the best of our knowledge, the first demonstration of centimeter-scale unidirectionally aligned single-crystalline ferrite films grown via CVD, marking a substantial advance beyond previously reported polycrystalline or randomly oriented domains.

To investigate the quality of CVD-synthesized CFO single-crystalline films, we conducted atomic-scale structural characterization of the transferred CFO films. High-resolution transmission electron microscopy (HRTEM) was employed to elucidate the detailed crystal structure of CFO films. As shown in Figure 1c, the well-defined hexagonal lattice pattern reveals the symmetry information of the CFO (111) plane. The measured interplanar spacing of 2.98 Å perfectly matches the theoretical value for the (220) plane, confirming both the surface characteristics of the (111) orientation and the excellent single crystallinity. Along the [111] zone axis, the selected-area electron diffraction (SAED) pattern exhibits only a single set of diffraction spots, further corroborating the single-crystalline nature. Quantitative energy-dispersive X-ray spectroscopy (EDS) analysis reveals an elemental ratio of 1:2.1:4.1, consistent with the stoichiometric composition of CFO (Figure S3, Supporting Information). Furthermore, high-angle annular dark-field scanning transmission electron microscopy (HAADF-STEM) was utilized to examine the atomic structure of CFO. As presented in Figure 1d,e, both plan-view and cross-sectional atomic images exhibit remarkable agreement with the standard atomic structure of CFO, demonstrating the high crystallographic quality of the synthesized films. These atomic-scale characterizations collectively confirm the exceptional structural integrity and chemical homogeneity of the CFO films, laying a solid foundation for their promising applications in advanced electronic and spintronic devices.

To deeply understand the mechanism of this morphological heterogeneity, we propose a comprehensive investigation through two complementary analytical lenses: the interface coupling and thermal dynamics. The realization of large-area single-crystal synthesis fundamentally relies on lattice symmetry matching between the substrate and the target material.^[28,29] Typically, crystallographic registry is preferentially established along high-symmetry substrate axes to minimize interfacial formation energy^[30], such as the (0001) plane of sapphire,^[31] <110> direction of Cu (111)^[32] and GaN (0001).^[33] Crucially, single-orientation growth is energetically favored only when the symmetry group of the substrate constitutes a subgroup of the target 2D material's symmetry group. Specifically, considering a 2D material with a G_{2D} symmetry group on a substrate with a symmetry group of G_{sub} , according to Lagrange's theorem of group theory,

Table 1. The number of equivalent but distinct alignments of CFO on various substrates.

G_{2D}	C_{3V}			
G_{sub}	C_{6V}	C_{4V}	C_{3V}	C_{2V}
$G_{2D@sub}$	C_{3V}	C_V	C_{3V}	C_V
$ G_{sub} $	12	8	6	4
$ G_{2D@sub} $	6	2	6	2
N	2	4	1	2

the number of equivalent but different orientations of 2D materials on the substrate can be expressed as^[30,34]:

$$N = \frac{|G_{sub}|}{|G_{2D@sub}|} \quad (1)$$

where $|G_{sub}|$ and $|G_{2D@sub}|$ are the numbers of symmetry operations of G_{sub} and $G_{2D@sub}$, respectively. We summarized the number of equivalent but distinct alignments of CFO on various substrates in Table 1 by considering all possible combinations of the symmetries of the CFO and substrate.

Fluorophlogopite mica was selected as the substrate due to its atomically flat layered structure derived from weak K⁺-mediated bonding between layers, enabling perfect (001)-plane cleavage.^[35] This vdW dielectric surface exhibits a distorted hexagonal symmetry: while the K⁺-terminated (001) face nominally possesses 6-fold rotational symmetry, subtle oxygen sublattice distortions reduce the effective surface symmetry to 3-fold,^[29] which is the same as that of CFO (111). Such symmetry degradation creates lattice symmetry matching that promotes unidirectional alignment of CFO nuclei while suppressing multidomain formation—a prerequisite enabling our observed large-area orientational uniformity. In contrast, we used c-plane sapphire, which is known with six-fold rotational symmetry, as the substrate to grow CFO. As shown in Figure S4 (Supporting Information), whether nucleation timing was before or after the temperature stabilized, antiparallel orientation growth emerged.

To theoretically validate the orientation selection mechanism, we performed density functional theory (DFT) calculations for CFO (111) domains on fluorophlogopite mica (001) substrates at varying rotational angles (see Experimental Section and Note S2, Supporting Information for details). In order to maintain the symmetry of the structure and the integrity of the crystallographic information, we chose to construct a diamond-shaped cluster structure when designing cluster structure. Figure 1f shows the nine heterojunction models with different rotational angles. As shown in Figure 1g, the binding energy profile exhibits two local minima at +30° and −30°, corresponding to antiparallel preferential orientations. Notably, the +30° configuration demonstrates slightly higher binding energy than the −30° configuration, confirming the energy preference for unidirectional alignment. However, the marginal energy difference between these orientations suggests that external perturbations, especially thermal perturbations during the heating process, could

induce sporadic antiparallel domain formation. It is noteworthy that the binding energy at -15° is lower than at 30° . This observation, however, does not imply that -15° is a preferred growth orientation compared to 30° . Within the framework of potential energy surface theory, a stable equilibrium point must satisfy two conditions simultaneously: a zero first derivative and a positive second derivative. Clearly, the -15° configuration fails to meet both criteria.

Gas flow dynamics serve as a critical determinant in governing the thermal kinetics of CVD, particularly for 2D materials.^[36] Extensive experimental studies have established that carrier gas flow parameters can precisely regulate key material properties, including morphological evolution, layer thickness, crystallographic orientation, and even interfacial registry in moiré superlattices. For instance, in 2D TMDC, directional flow control enables deterministic selection between in-plane monolayer expansion and vertical bilayer stacking, while simultaneously tuning nucleation sites and rotational alignment.^[37] Significantly, such flow-mediated growth manipulation has been extended to non-vdW materials like $\text{Bi}_2\text{O}_2\text{Se}$,^[38] demonstrating the universality of this approach. The flow velocity is inversely proportional to the boundary layer thickness. During deposition, the precursor must diffuse across this boundary layer to reach the substrate surface. At lower flow velocities, the boundary layer thickness increases, leading to a lower precursor concentration within the boundary layer. To prove this, we conduct CVD under different gas flow rates, as shown in Figure S5 (Supporting Information). With the increase of gas flow rate, both the size and quantity of CFO domains increase significantly. This result clearly indicates that a low flow rate during the temperature ramp phase does not trigger nucleation. Therefore, we employ flow-switching between high/low-flows (150/10 sccm) to control nucleation initiation/suppression while maintaining Ar atmosphere integrity. Our systematic investigation reveals a strong correlation between nucleation timing and growth orientation. Figure 2a illustrates two different gas-flow modulation routes. (R_i) meaning nucleation happens after thermal equilibrium yields $\approx 100\%$ unidirectionally aligned triangular domains throughout the mica, as illustrated in Figure 2b and Figure S6 (Supporting Information). Observably, we implemented an intentional 5-min low-flow (10 sccm) stabilization period upon reaching the growth temperature prior to initiating the main deposition phase. This pre-coalescence protocol ensures complete precursor melting and promotes spatially uniform distribution of precursors compared to their solid powder state, thereby facilitating a relatively homogeneous precursor flux reaching different positions of the mica. Second harmonic generation (SHG) measurement was conducted to demonstrate the unidirectional growth feature of CFO films through R_i (Figure 2f). Furthermore, the SHG of two domains with the same orientation showed no detailed intensity attenuation across the grain boundary, confirming the seamless stitching of two CFO domains. The polarized-SHG spectra of two merged CFO domains (Figure S7, Supporting Information) exhibit nearly identical hexapolar patterns, which is consistent with the symmetry information of the $Fd-3m$ space group of CFO, providing strong evidence for the 3-fold rotational symmetry of the CFO (111). In contrast, conventional CVD protocols initiating nucleation during the temperature ramping up (R_{II}) produce CFO domains with bidirectional triangular orientations (60° ro-

tational variants) and sporadic hexagonal thick flakes (Figure 2c). To directly analyze how nucleation timing regulation influenced growth orientation, we conducted a statistical analysis of orientation distribution patterns, as shown in Figure 2d,e.

This morphological heterogeneity arises from stochastic nucleation events under thermally unstable conditions, where transient precursor supersaturation drives kinetic competition between surface energy minimization and defect-assisted growth. Under non-isothermal conditions, the chemical potential difference ($\Delta\mu$) governing the epitaxial growth process exhibits dynamic behavior due to temperature-dependent phase equilibria. During the heating phase, the temperature difference between the substrate and precursor source evolves with time. Assuming linear heating rates, a time-dependent chemical potential difference is expressed as^[29]:

$$\Delta\mu = \frac{\Delta H}{T} \cdot \Delta T \quad (2)$$

where ΔH is the enthalpy change of the phase transition, T is the temperature evolving linearly with time t , and ΔT is the temperature difference between the product and the precursor powder. The $\Delta\mu$ is non-zero and disturbed with time because the substrate and precursor cannot completely keep the same change with temperature, which results in a non-equilibrium process energetically in favor of bidirectional growth. As the system approaches thermal equilibrium, the temperature difference between the product and the precursor powder becomes negligible ($\Delta T \ll T$), reducing $\Delta\mu$ to near-zero. In this regime, the growth transitions to a thermodynamically dominated quasi-equilibrium process. The slight energy difference between the two metastable orientations is magnified under low $\Delta\mu$, enabling robust selection of the single lowest-energy orientation. In the meantime, the K^+ at the surface of cleaved fluorphlogopite mica is easily removed during annealing processes, which is reported in a previous study. DFT calculation of CFO (111) domains on K^+ defects-enriched fluorphlogopite mica was conducted (Figure S8, Supporting Information), revealing a significantly amplified energy difference of ≈ 0.5 eV between -30° and 30° . Thus, the defect-enriched surface will further exacerbate the antiparallel energy degeneracy, which plays a second driving force of unidirectional growth.

For achieving precise control over CFO film coverage and complete domains coalescence, we systematically investigated growth time as a critical kinetic control parameter. While extended growth durations are widely reported to promote lateral expansion in 2D materials, our time-dependent study establishes quantitative correlations between deposition kinetics and interfacial stitching quality. Figure 2e presents a comparative analysis of CFO films synthesized at ≈ 5 , ≈ 10 , ≈ 15 , and ≈ 20 min growth intervals through atomic force microscopy (AFM) and optical microscopy (OM) characterization. The progressive evolution from isolated triangular domains (≈ 5 min) to fully coalesced single-crystalline films (≈ 20 min) demonstrates a self-limited lateral growth mechanism dominated by surface diffusion. The thickness increases from 5.8 to 54.5 nm as the growth time extends from 5 to 50 min, as shown in Figure S9 (Supporting Information).

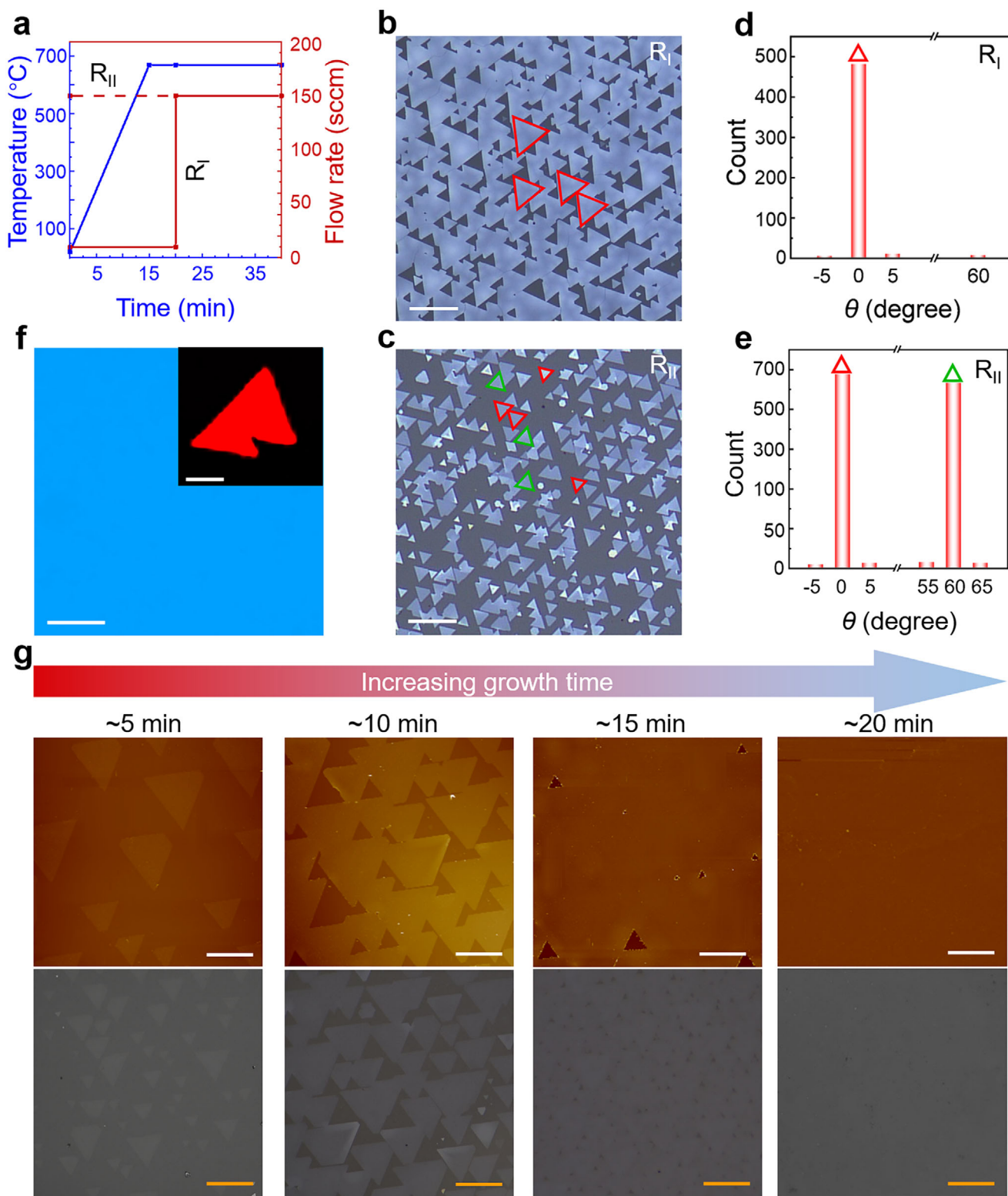


Figure 2. Growth mechanism of unidirectional CFO on mica. a) Temperature (blue) and flow rate (red) vs time in R_I and R_{II} . b, c) OM image of as-grown CFO domains under R_I and R_{II} , respectively. Scale bars: 60 μm . d, e) Statistical analysis of the orientations of CFO domains on mica in (b, c), respectively. f) SHG mapping of CFO film. Scale bar: 20 μm . Inset: SHG mapping of two unidirectional CFO domains merged on mica. Scale bar: 10 μm . g) AFM (up) and OM (down) images of CFO films on mica with growth times of ~ 5 , ~ 10 , ~ 15 , and ~ 20 min, respectively. Scale bars: 20 μm (up) and 35 μm (down).

Additionally, a comprehensive investigation of growth temperature effects reveals distinct thermodynamic regimes governing CFO domains evolution. As depicted in Figure S10 (Supporting Information), at low growth temperatures, the domains exhibit a random orientation, which is consistent with the previously demonstrated random nucleation at lower temperatures. It is worth noting that with an increase in growth temperature, the lateral size of the CFO domains decreases, while their thickness gradually increases. Furthermore, the number of domains increases with elevated temperatures, which can be attributed to variations in precursor supersaturation. Higher temperatures result in higher supersaturation, and under such conditions, excess energy is converted into surface energy of the crystals, in accordance with the principle of energy conservation. Consequently, the number of domains increases, and their size diminishes to enhance the total surface energy of the system at equilibrium. This behavior is further substantiated by varying the FeCl_3 concentration in the precursor, which lowers the melting point and increases the precursor concentration within the system. As shown in Figure S11 (Supporting Information), in the absence of FeCl_3 , no domains are deposited, as the precursor is unable to dissolve. However, with increasing amounts of FeCl_3 , from optimal to excessive concentrations, the resulting supersaturation leads to an increase in the number of domains and a reduction in their size. Additionally, the appearance of a small number of domains with pyramidal-type thickness on the substrate further supports the initiation of the layer-by-layer (LBL) growth mode triggered by the increased supersaturation.^[39] In conclusion, through precise control over the growth time, temperature, and FeCl_3 concentration, we have achieved a multi-dimensional control over the orientation, size, and thickness of CFO domains, ultimately enabling the seamless integration of single-crystalline films. In order to verify the reproducibility of our growth method, we performed five successive experiments to synthesize films on a mica, which demonstrates the great reproducibility in the growth method, as shown in Figure S12 (Supporting Information). It is worth mentioning that to show the universality of the synthesis strategy in complex oxides, we extend the successful case to other spinel ferrites, such as MnFe_2O_4 and NiFe_2O_4 , as depicted in Figures S13, S14 (Supporting Information). To definitively demonstrate the ferrite films' uniformity, AFM was performed on five distinct regions of the film samples, all confirming excellent homogeneity (Figures S15–S17, Supporting Information).

To further assess the spatial homogeneity and single-crystalline feature, multiple characterizations were carried out. X-ray diffraction (XRD) patterns in Figure 3a verify epitaxial growth along the (111) crystallographic plane, coinciding with the standard PDF card. The blue dashed lines mark XRD peaks of the (111), (222), (333), (444) planes of CFO, while the yellow dashed lines are attributed to mica. Raman spectroscopy was performed over a $0.5 \times 0.5 \text{ mm}^2$ region (Figure 3b,c) where four prominent Raman peaks are observed at 692.7, 620.2, 470.6, and 304.8 cm^{-1} , which correspond to its A_{1g}^1 , A_{1g}^2 , T_{1g}^1 and E_g modes, respectively, demonstrating remarkable consistency in characteristic peak positions and intensities along both X- and Y-directions. The high-frequency A_{1g} vibrational modes primarily arise from oxygen atom movements within the Co-tetrahedral units, whereas the lower-frequency modes, T_{1g} and E_g , corre-

spond to vibrations associated with the Fe-octahedral structures, which is consistent with previous research.^[15,40] X-ray photoelectron spectroscopy (XPS) analysis confirms the desired chemical composition and valence states (Figure S18, Supporting Information). The binding energies at ≈ 796.4 and $\approx 780.3 \text{ eV}$ are attributed to Co^{2+} , while the peaks of ≈ 725.9 and $\approx 712.3 \text{ eV}$ are assigned to Fe^{3+} , and the two O^{2-} peaks are located at 529.6 and 531.1 eV.^[41] Notably, ≈ 803 and $\approx 786 \text{ eV}$ are identified as the Co $2p_{3/2}$ and Co $2p_{1/2}$ satellite peaks, respectively. Similarly, the features at ≈ 733 and $\approx 718 \text{ eV}$ correspond to the Fe $2p_{3/2}$ and Fe $2p_{1/2}$ satellite peaks, respectively. The single-crystalline nature was further corroborated by electron backscatter diffraction (EBSD) measurements. As shown in Figure 3d, the inverse pole figure (IPF) mappings across X-, Y-, and Z-directions (1 mm scale bar), uniform color distributions, and consistent orientation intensities were observed in all three orthogonal directions. The crystal orientation without twinning and grain boundary not only confirms the single-crystalline character but also validates the (111)-oriented growth mode. In addition, electron backscattered patterns (EBSPs) collected at nine different positions across a $1 \times 1 \text{ mm}^2$ area show only one set of Kikuchi patterns, indicating the same crystal orientation (Figure 3f). The combined structural and compositional analyses demonstrate that our CVD-derived CFO films exhibit exceptional crystalline quality and spatial uniformity, meeting critical requirements for industrial-scale applications in advanced electronic devices, where magnetic anisotropy and coercive field must remain invariant over large lateral areas.

As a unique member of the spinel family, CFO exhibits distinctive magnetic properties arising from the intricate interplay of spin, electronic, and orbital degrees of freedom. To demonstrate the superior magnetic characteristics of CFO single-crystalline films and to comprehensively evaluate the magnetic properties of our synthesized single-crystalline CFO films, we performed vibrating sample magnetometry (VSM) measurements, characterizing both in-plane and out-of-plane magnetic configurations. A single CFO/mica sample was sectioned into multiple $2 \times 2 \text{ mm}^2$ square flakes. Flakes exhibiting non-uniform thickness or excessive impurities were selectively removed. This careful selection process ensures that the films used for subsequent measurements possess highly comparable thickness. Figure 4a,b presents the temperature-dependent magnetization curves under field-cooled (FC) and zero-field-cooled (ZFC) conditions from 300 to 900 K, with applied magnetic fields in both out-of-plane and in-plane orientations. Remarkably, even at elevated temperatures, our CFO films exhibit exceptionally high magnetization with clearly distinguishable FC and ZFC curves in both configurations, indicating ferrimagnetic behavior that persists up to $\approx 730 \text{ K}$. This suggests a Curie temperature (T_C) significantly above room temperature. The differential analysis of the ZFC curve reveals a distinct minimum at $\approx 730 \text{ K}$ (Figure S19, Supporting Information), confirming the exceptionally high T_C of CFO films. To further validate this finding, we measured magnetization hysteresis loops at various temperatures. As shown in Figure 4c,d, the CFO films demonstrate robust hysteresis in both in-plane and out-of-plane configurations, with coercive fields gradually decreasing and magnetization diminishing as temperature increases, completely vanishing at 800 K, consistent with the ZFC differential analysis. Notably, the in-plane configuration exhibits higher magnetization and larger coercive fields, which contrasts

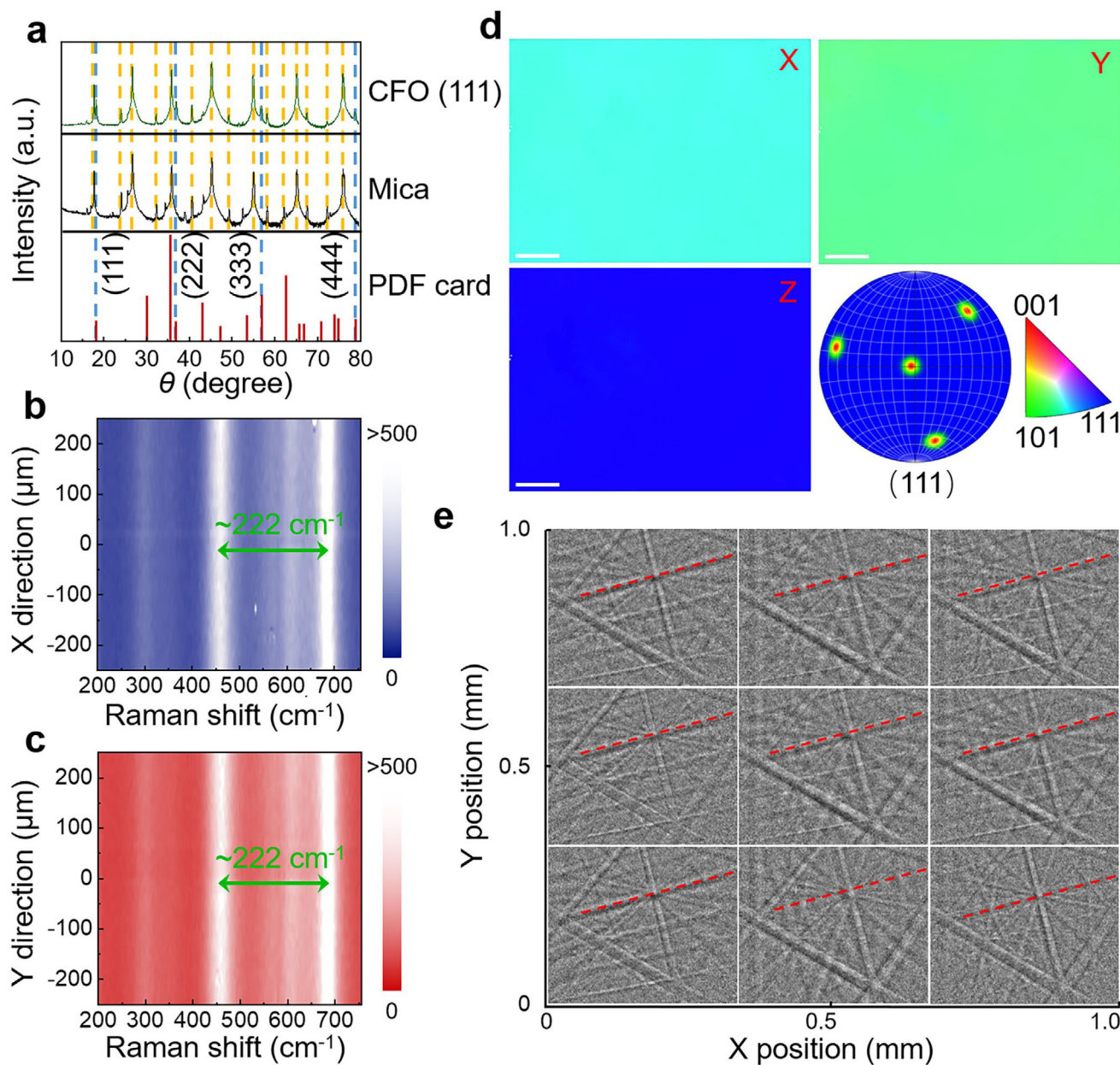


Figure 3. Crystalline quality of CVD-synthesized single-crystalline CFO films. a) XRD pattern of as-grown CFO (111) on mica, demonstrating the epitaxial nature with (111) preferred orientation. b, c) Color-code images of Raman line scan mapping along the X and Y directions. d) EBSD IPF maps extracted from as-grown CFO (111) in spatial X, Y, and Z directions. Scale bars: 100 μm . The identical IPF maps in-plane (X and Y directions) confirm the crystal orientation without twinning, while the pole figure indicates the normal stacking direction (111). e) EBSPs extracted from nine different positions across a $1 \times 1 \text{ mm}^2$ area, showing only one set of Kikuchi patterns.

with previous reports of out-of-plane magnetic easy axis preference in CFO (111) at low temperatures. We attribute this phenomenon to thermally induced structural relaxation in CFO (111) at high temperatures, generating oxygen vacancies that create compressive strain, thereby reorienting the magnetic easy axis from out-of-plane to in-plane.^[42] We performed XPS analysis on both the as-grown and post-annealed CFO to characterize the O 1s core level, as shown in Figure S20 (Supporting Information). The O_I peak, corresponding to lattice oxygen, exhibits a clear shift toward higher binding energy upon annealing, mov-

ing from 529.21 eV (as-grown) to 529.86 eV (post-annealed). In contrast, the position of the O_{II} peak, associated with surface oxygen species, remains virtually unchanged. This shift in the lattice oxygen binding energy can be explained by the formation of oxygen vacancies. These vacancies create localized positive charge centers within the lattice. This positive potential acts to repel valence electrons, leading to an overall upward shift in the Fermi level and a consequent reduction in the work function. The reduction in work function signifies a decrease in the energy required to extract electrons from the material, indicating that an

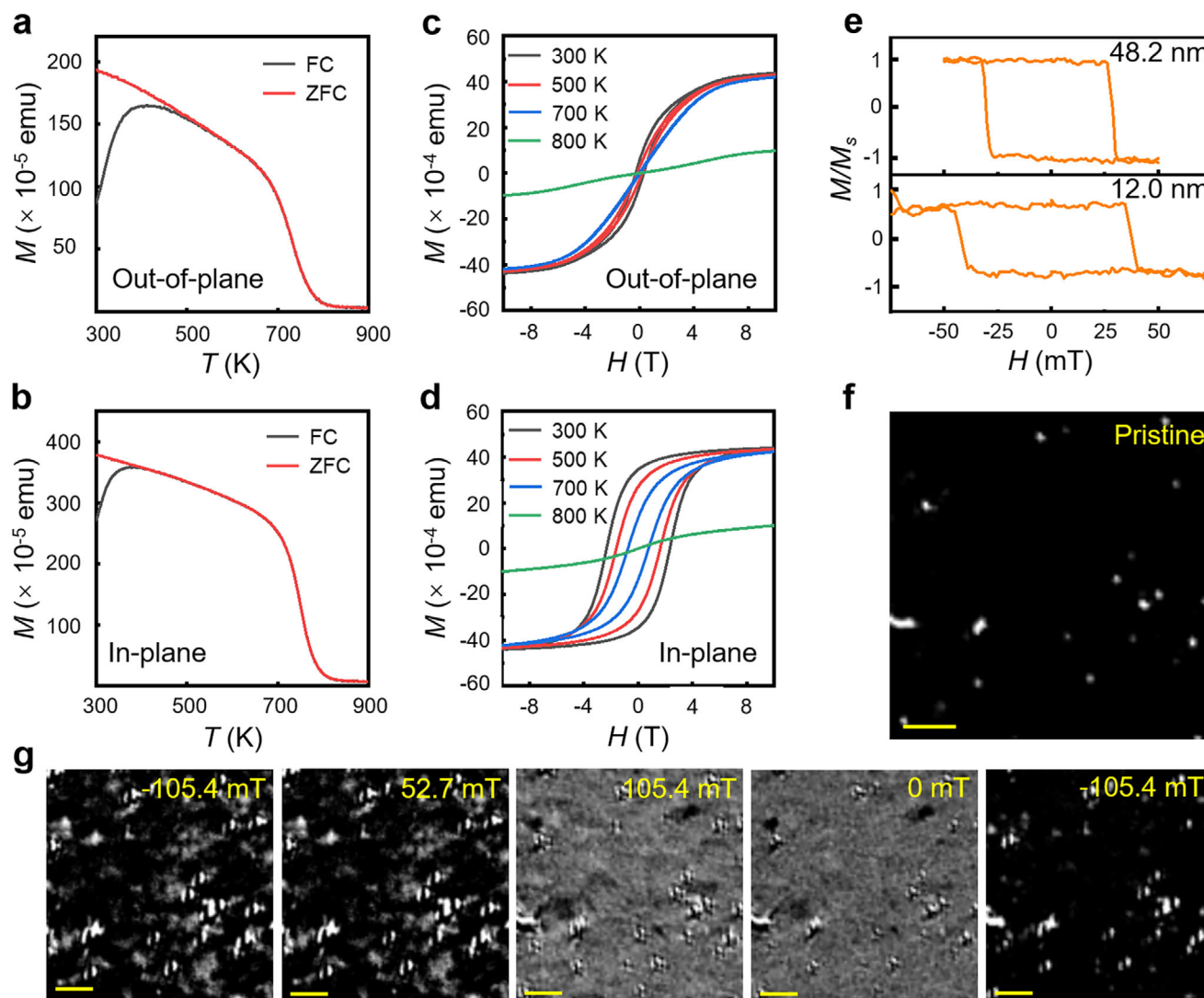


Figure 4. Magnetic characterization of as-grown CFO films. a, b) Temperature dependence of magnetic susceptibility under out-of-plane (OOP) and in-plane (IP) magnetic fields of 0.1 T, respectively. c, d) Magnetic hysteresis loops of CFO films measured at different temperatures under OOP and IP magnetic fields, respectively. e) MOKE hysteresis loops of CFO film with different thicknesses. f) Pristine MOKE microscopy image of a typical CFO film. Scale bar: 10 μ m. g) MOKE microscopy images of the same CFO film during bidirectional magnetic field sweeping. Scale bars: 10 μ m.

increased binding energy is measured for the lattice oxygen. Following annealing, the oxygen atoms outgas. Concurrently, interfacial interaction with the mica substrate, similarly observed in spinel Fe_3O_4 (111) nanosheets,^[28] induces out-of-plane compressive strain in the CFO lattice. Given that CFO possesses a negative magnetostriction, its magnetic moments tend to align parallel to the film plane to counteract this compressive strain, resulting in the establishment of an in-plane magnetic easy axis.

In order to investigate the hard magnetic properties and visualize the magnetic domain behavior, we employed magnetooptical Kerr effect (MOKE) microscopy, a non-invasive technique ideal for studying 2D magnetic materials. At room temperature, we measured hysteresis loops for CFO films with thicknesses of 48.2 and 12.0 nm (Figure 4e), both exhibiting non-zero remanent magnetization at zero field and nearly square hysteresis loops, indicative of strong hard magnetic properties and out-of-plane easy

axis alignment at room temperature. AFM images at six different positions on the 48.2 nm and 12 nm samples indicate maximum thickness deviations of ≈ 2.2 and ≈ 1.8 nm, respectively (Figures S21, S22, Supporting Information). These values demonstrate excellent thickness uniformity across both samples. We also summarized the coercive field (H_C) evolution as a function of thickness (Figure S23, Supporting Information). As the thickness increases from 8.3 to 54.5 nm, H_C decreases from 75 to 22.5 mT. This exhibits a clear thickness-dependent effect, suggesting an enhancement of perpendicular magnetic anisotropy (PMA). It is worth noting that the sub-10 nm films exhibit robust magnetic hysteresis loops at room temperature with significantly large H_C , aligning with the thicknesses used in 2D spintronic devices.^[43,44] For direct visualization of the out-of-plane magnetic behavior, we captured MOKE mapping of a selected film region during bidirectional magnetic field sweeping (Figure 4g). Pristine MOKE

microscopy image demonstrated a uniform spontaneous magnetization (Figure 4f). After saturating the magnetization with a high field, we reversed the field direction. The mapping reveals that the overall magnetization remains largely unchanged until the field exceeds a critical value (coercive field), at which point the contrast completely reverses, indicating magnetization flipping to saturation. Subsequent reverse sweeping exhibits analogous behavior, demonstrating that the CFO film maintains a single-domain magnetic structure even after coalescence. This uniform switching behavior, coupled with the large coercive field, highlights the tremendous potential of our CFO films for applications and underscores their advantages for large-scale spintronic device integration.

Currently, nearly all integrated circuits are fundamentally based on silicon technology. However, as previously discussed, CFO (111) faces challenges in lattice matching and symmetry compatibility with established silicon-based processes. Although studies have demonstrated the transfer of 2D CFO (111) onto silicon wafers, this approach inevitably introduces wrinkles and surface contamination. Ideally, direct epitaxial growth of high-quality materials on silicon would be the optimal solution. We conducted direct growth on bare silicon substrates yielded only irregularly shaped particles (Figure S24a, Supporting Information). To address the inherent surface disorder of silicon substrates and enable long-range ordered single-crystalline growth, the introduction of a functional vdW buffer layer—either through transfer or in situ growth—may provide a viable pathway for silicon-based integration of 2D CFO (111).^[45] Therefore, we implemented a mechanically exfoliated mica buffer layer on silicon substrates. However, the underlying substrate can still influence the epilayer via long-range interactions.^[46] The four-fold rotational symmetry of the Si (100) substrate leads to the formation of two equivalent but distinct alignments in the CFO domains, as shown in Figure S24b (Supporting Information). To minimize this interaction between the Si substrate and the epilayer, CFO domains grown on a thicker mica buffer layer exhibit significantly enhanced unidirectional, as evidenced in Figure S24c (Supporting Information). The CFO domains on mica/SiO₂ show the same structural and magnetic properties as those grown directly on bare mica (Figure S24d,e, Supporting Information). Unfortunately, there remains room for improvement in thickness uniformity, and the selective removal process for the mica buffer layer remains technically unfeasible at this stage. Another attempt is to utilize thermal release tape to delaminate the CFO film onto a flexible, bendable substrate. This enables the subsequent transfer of the CFO film onto virtually any desired substrate (Figure S25, Supporting Information).

A current limitation of our growth method is the difficulty in achieving film thicknesses below 10 nm following seamless coalescence, primarily due to the isotropic growth behavior of CFO. This presents a significant challenge for the large-area growth of nonlayered materials. Addressing this limitation will necessitate considerable future research and experimentation. Currently, we propose two potential strategies to mitigate this issue: 1) The first strategy involves leveraging a thermodynamics-triggered competitive growth model to control the competition between lateral and vertical growth of domains, delaying vertical growth and reducing the thickness of individual domains.^[47] This aims to achieve a limited thickness increase upon achieving seamless co-

alescence. 2) The second strategy focuses on minimizing overall growth time. In the context of device integration, implementing patterned growth can achieve a similar outcome.^[48,49] This approach can drastically shorten the required growth time per unit within the array, thereby facilitating further reductions in film thickness.

3. Conclusion

In summary, this study achieved centimeter-scale growth of ultrathin single-crystalline CFO films on mica. A precisely engineered nucleation timing ensured unidirectional alignment and seamless coalescence. Structural characterization (Raman, XRD, EBSD) validated epitaxial (111)-oriented growth and stoichiometric uniformity, and magnetic analysis (VSM, MOKE) confirmed robust ferrimagnetism up to 730 K, with thickness-dependent coercivity and single-domain behavior. The work establishes a scalable framework for synthesizing large-area 2D magnetic materials, addressing critical challenges in domain control and thermal stability. These findings advance the application of CFO in high-temperature spintronic devices and provide insights into symmetry-driven epitaxy for complex oxides.

4. Experimental Section

Sample Synthesis and Transfer. The synthesis was carried out using an atmospheric pressure CVD (APCVD) system equipped with a 1-inch quartz tube. For the CFO growth, 20 mg of ferric oxide (α -Fe₂O₃, 99.5%, Aladdin), 20 mg of cobaltous oxide (CoO, 99.99%, Aladdin), 5 mg ferric chloride (FeCl₃, 99.99%, Sigma-Aldrich), and 3 mg sodium chloride powder were mixed evenly and used as precursors. A quartz boat with precursor powders was placed in the center of the heating zone of the furnace, with fluorophlogopite mica substrates arrayed on the above. The quartz tube was purged with high-purity argon gas (Ar, 99.999%) at a flow rate of 500 sccm for 10 min. Then, the furnace was first heated from room temperature to 670 °C in 15 min and maintained at this temperature for another 5 min for complete precursor melting with 10 sccm high-purity Ar. After that, 150 sccm Ar flow was used as the carrier gas to provide a suitable atmosphere for CFO growth. After the reaction was completed, the furnace naturally cooled down to room temperature. Eventually, CFO single-crystalline films were deposited on the bottom surface of mica substrates. For the MFO/NFO growth, 20 mg of ferric oxide (α -Fe₂O₃, 99.5%, Aladdin), 20 mg of manganous oxide (MnO, 99%, Bide)/nickel oxide (NiO, 99.99%, Aladdin), 5 mg ferric chloride (FeCl₃, 99.99%, Sigma-Aldrich) and 3 mg sodium chloride powders were mixed evenly and used as precursors. The other growth condition was the same as that for CFO. For the sample transfer, polystyrene (PS) was spin-coated onto the sample (3000 rpm, 60 s) at first, followed by baking at 120 °C for 30 min. Then, the PS-capped sample film was lifted off in the deionized water, followed by supporting the film with the required substrates (such as a molybdenum grid). The substrate with ferrite film on the surface was dried at 100 °C for 10 min. Finally, methylbenzene was used to remove the PS.

Sample Characterization: The morphology, thickness, and material quality of ferrite films were characterized by OM (Olympus BX51M), AFM (Bruker Dimension Icon), and Raman spectra (Horiba, 532 nm excitation laser) under the atmospheric environment, respectively. HAADF-STEM imaging measurements were taken at 300 kV on a FEI-Titan Cubed Themis G2 300 instrument equipped with a double spherical aberration corrector. TEM imaging, SAED pattern, and EDS measurements were performed on a JEM-F200. Magnetic measurements were performed by a physical property measurement system (PPMS, Quantum Design) equipped with vibrating sample magnetometry utility, and a Kerr microscope with 617 nm wavelength LED (TuoTuo Technology, TTT-03).

Theoretical Calculations: All results of calculations in this work were performed in the framework of the density functional theory (DFT) with the projector augmented plane-wave method, as implemented in the Vienna ab initio simulation package (VASP). The generalized gradient approximation proposed by Perdew–Burke–Ernzerhof (PBE) was selected for the exchange–correlation potential. The cut-off energy for a plane wave was set to 480 eV. The energy criterion was set to 10^{-5} eV in the iterative solution of the Kohn–Sham equation. All the structures were relaxed until the residual forces on the atoms have declined to less than $0.02 \text{ eV } \text{\AA}^{-1}$. A 15 \AA vacuum was applied to expose the surface. The adsorption energy E_{bind} is described as follows:

$$E_{\text{bind}} = E_{\text{total}} - E_{\text{slabA}} - E_{\text{slabB}} \quad (3)$$

Here, the E_{total} is the total energy of the heterojunction, E_{slabA} and E_{slabB} are the energies of the two slab structures.

Supporting Information

Supporting Information is available from the Wiley Online Library or from the author.

Acknowledgements

Y.Z. and R.C. contributed equally to this work. This work was supported by the National Natural Science Foundation of China (Nos. 62274121, 92464303, U23A20364, and 623B2078), the Wuhan Industrial Innovation Joint Laboratory (No. 2024050902040443), the National Key R&D Program (No. 2022YFA1402503), and the Undergraduate Training Programs for Innovation of Wuhan University.

Conflict of Interest

The authors declare no conflict of interest.

Data Availability Statement

The data that support the findings of this study are available from the corresponding author upon reasonable request.

Keywords

2D ferrites, centimeter scale, high Curie temperature, Van der Waals epitaxy

Received: May 13, 2025
Revised: July 17, 2025
Published online:

- [1] C. Gong, X. Zhang, *Science* **2019**, 363, 706.
- [2] Y. Deng, Y. Yu, Y. Song, J. Zhang, N. Z. Wang, Z. Sun, Y. Yi, Y. Z. Wu, S. Wu, J. Zhu, J. Wang, X. H. Chen, Y. Zhang, *Nature* **2018**, 563, 94.
- [3] E. Dagotto, *Rev. Mod. Phys.* **1994**, 66, 763.
- [4] B. Huang, G. Clark, E. Navarro-Moratalla, D. R. Klein, R. Cheng, K. L. Seyler, D. Zhong, E. Schmidgall, M. A. McGuire, D. H. Cobden, W. Yao, D. Xiao, P. Jarillo-Herrero, X. Xu, *Nature* **2017**, 546, 270.
- [5] D. R. Klein, D. MacNeill, J. L. Lado, D. Soriano, E. Navarro-Moratalla, K. Watanabe, T. Taniguchi, S. Manni, P. Canfield, J. Fernández-Rossier, P. Jarillo-Herrero, *Science* **2018**, 360, 1218.

- [6] Z. Sun, Y. Yi, T. Song, G. Clark, B. Huang, Y. Shan, S. Wu, D. Huang, C. Gao, Z. Chen, M. McGuire, T. Cao, D. Xiao, W. T. Liu, W. Yao, X. Xu, S. Wu, *Nature* **2019**, 572, 497.
- [7] D. P. Kozlenko, O. N. Lis, N. T. Dang, S. E. Kichanov, E. V. Lukin, I. Y. Zel, N. O. Golosova, B. N. Savenko, T. L. Phan, T. K. Dinh, T. A. Tran, *ChemPhysMater* **2025**, 4, 280.
- [8] G. Zhang, F. Guo, H. Wu, X. Wen, L. Yang, W. Jin, W. Zhang, H. Chang, *Nat. Commun.* **2022**, 13, 5067.
- [9] S. Wu, Z. He, M. Gu, L. Ren, J. Li, B. Deng, D. Wang, X. Guo, W. Li, M. Chen, Y. Chen, M. Meng, Q. Ye, B. Shen, X. Chen, J. Guo, G. Xing, I. K. Sou, S. Li, *Nat. Commun.* **2024**, 15, 10765.
- [10] M. Wang, B. Lei, K. Zhu, Y. Deng, M. Tian, Z. Xiang, T. Wu, X. Chen, *npj 2D Mater. Appl.* **2024**, 8, 22.
- [11] C. Gong, L. Li, Z. Li, H. Ji, A. Stern, Y. Xia, T. Cao, W. Bao, C. Wang, Y. Wang, Z. Q. Qiu, R. J. Cava, S. G. Louie, J. Xia, X. Zhang, *Nature* **2017**, 546, 265.
- [12] L. Kang, C. Ye, X. Zhao, X. Zhou, J. Hu, Q. Li, D. Liu, C. M. Das, J. Yang, D. Hu, J. Chen, X. Cao, Y. Zhang, M. Xu, J. Di, D. Tian, P. Song, G. Kuttly, Q. Zeng, Q. Fu, Y. Deng, J. Zhou, A. Ariando, F. Miao, G. Hong, Y. Huang, S. J. Pennycook, K. T. Yong, W. Ji, X. Wang, et al., *Nat. Commun.* **2020**, 11, 3729.
- [13] D. Lei, N. Hu, L. Wu, Alamusi, H. Ning, Y. Wang, Z. Jin, Y. Liu, *Nano Mater. Sci.* **2024**, 6, 201.
- [14] G. Hu, J. H. Choi, C. B. Eom, V. G. Harris, Y. Suzuki, *Phys. Rev. B* **2000**, 62, R779.
- [15] R. Cheng, L. Yin, Y. Wen, B. Zhai, Y. Guo, Z. Zhang, W. Liao, W. Xiong, H. Wang, S. Yuan, J. Jiang, C. Liu, J. He, *Nat. Commun.* **2022**, 13, 5241.
- [16] J. Zhou, J. Lin, X. Huang, Y. Zhou, Y. Chen, J. Xia, H. Wang, Y. Xie, H. Yu, J. Lei, D. Wu, F. Liu, Q. Fu, C. H. Hsu, C. Yang, L. Lu, T. Yu, Z. Shen, H. Lin, B. I. Yakobson, Q. Liu, K. Suenaga, G. Liu, Z. Liu, *Nature* **2018**, 556, 355.
- [17] K. S. Burch, D. Mandrus, J. G. Park, *Nature* **2018**, 563, 47.
- [18] K. F. Mak, J. Shan, D. C. Ralph, *Nat. Rev. Phys.* **2019**, 1, 646.
- [19] L. Yin, R. Cheng, X. Wan, J. Ding, J. Jia, Y. Wen, X. Liu, Y. Guo, J. He, *Nat. Mater.* **2025**, 24, 197.
- [20] Y. Liu, X. Duan, H. J. Shin, S. Park, Y. Huang, X. Duan, *Nature* **2021**, 591, 43.
- [21] P. Zubko, S. Gariglio, M. Gabay, P. Ghosez, J. M. Triscone, *Annu. Rev. Condens. Matter Phys.* **2011**, 2, 141.
- [22] J. Peng, Z. Chen, B. Ding, H. Cheng, *Research* **2023**, 6, 0040.
- [23] L. Yin, R. Cheng, Y. Wen, B. Zhai, J. Jiang, H. Wang, C. Liu, J. He, *Adv. Mater.* **2022**, 34, 2108313.
- [24] Y. Wang, J. C. Kim, Y. Li, K. Y. Ma, S. Hong, M. Kim, H. S. Shin, H. Y. Jeong, M. Chhowalla, *Nature* **2022**, 610, 61.
- [25] S. Wang, J. Crowther, H. Kageshima, H. Hibino, Y. Taniyasu, *ACS Nano* **2021**, 15, 14384.
- [26] Y. Zhang, L. Shen, M. Liu, X. Li, X. Lu, L. Lu, C. Ma, C. You, A. Chen, C. Huang, L. Chen, M. Alexe, C. L. Jia, *ACS Nano* **2017**, 11, 8002.
- [27] L. Huang, Z. Hu, H. Jin, J. Wu, K. Liu, Z. Xu, J. Wan, H. Zhou, J. Duan, B. Hu, J. Zhou, *Adv. Funct. Mater.* **2020**, 30, 1908486.
- [28] P. Wang, J. Ge, J. Luo, H. Wang, L. Song, Z. Li, J. Yang, Y. Wang, R. Du, F. Wang, J. Wang, J. He, J. Shi, *Nano Lett.* **2023**, 23, 1758.
- [29] K. Si, Y. Zhao, P. Zhang, X. Wang, Q. He, J. Wei, B. Li, Y. Wang, A. Cao, Z. Hu, P. Tang, F. Ding, Y. Gong, *Nat. Commun.* **2024**, 15, 7471.
- [30] J. Dong, L. Zhang, X. Dai, F. Ding, *Nat. Commun.* **2020**, 11, 5862.
- [31] Q. Ji, M. Kan, Y. Zhang, Y. Guo, D. Ma, J. Shi, Q. Sun, Q. Chen, Y. Zhang, Z. Liu, *Nano Lett.* **2015**, 15, 198.
- [32] J. Dong, L. Zhang, K. Zhang, F. Ding, *Nanoscale* **2018**, 10, 6878.
- [33] D. Ruzmetov, K. Zhang, G. Stan, B. Kalanyan, G. R. Bhimanapati, S. M. Eichfeld, R. A. Burke, P. B. Shah, T. P. O'Regan, F. J. Crowne, A. G. Birdwell, J. A. Robinson, A. V. Davydov, T. G. Ivanov, *ACS Nano* **2016**, 10, 3580.
- [34] W. Wang, Y. Zhang, W. Wang, M. Luo, Y. Meng, B. Li, Y. Yan, D. Yin, P. Xie, D. Li, D. Chen, Q. Quan, S. Yip, W. Hu, J. C. Ho, *Matter* **2024**, 7, 2236.

- [35] H. K. Christenson, N. H. Thomson, *Surf. Sci. Rep.* **2016**, *71*, 367.
- [36] S. Yuan, Y. Zhou, L. Yin, X. Wang, S. Jiang, Z. Song, Y. Wen, R. Cheng, J. He, *Adv. Phys. Res.* **2025**, *4*, 2400169.
- [37] J. Zhou, H. Huang, Z. Zhao, Z. Dou, L. Zhou, T. Zhang, Z. Huang, Y. Feng, D. Shi, N. Liu, J. Yang, J. C. Nie, Q. Wang, J. Dong, Y. Liu, R. Dou, Q. Xue, *Adv. Mater.* **2024**, *36*, 2408227.
- [38] X. Yang, Q. Zhang, Y. Song, Y. Fan, Y. He, Z. Zhu, Z. Bai, Q. Luo, G. Wang, G. Peng, M. Zhu, S. Qin, K. Novoselov, *ACS Appl. Mater. Interfaces* **2021**, *13*, 49153.
- [39] F. Meng, S. A. Morin, A. Forticaux, S. Jin, *Acc. Chem. Res.* **2013**, *46*, 1616.
- [40] Y. Liao, Y. Li, Z. Hu, J. Chu, *Appl. Phys. Lett.* **2012**, *100*, 071905.
- [41] K. J. Kim, J. Park, *J. Sol-Gel Sci. Technol.* **2019**, *92*, 40.
- [42] S. E. Shirsath, X. Liu, Y. Yasukawa, S. Li, A. Morisako, *Sci. Rep.* **2016**, *6*, 30074.
- [43] W. Zhu, Y. Zhu, T. Zhou, X. Zhang, H. Lin, Q. Cui, F. Yan, Z. Wang, Y. Deng, H. Yang, L. Zhao, I. Žutić, K. D. Belashchenko, K. Wang, *Nat. Commun.* **2023**, *14*, 5371.
- [44] Z. Wang, D. Sapkota, T. Taniguchi, K. Watanabe, D. Mandrus, A. F. Morpurgo, *Nano Lett.* **2018**, *18*, 4303.
- [45] R. Cheng, H. S. Kum, J. He, *Sci. Bull.* **2023**, *68*, 1087.
- [46] Y. Kim, S. S. Cruz, K. Lee, B. O. Alawode, C. Choi, Y. Song, J. M. Johnson, C. Heidelberger, W. Kong, S. Choi, K. Qiao, I. Almansouri, E. A. Fitzgerald, J. Kong, A. M. Kolpak, J. Hwang, J. Kim, *Nature* **2017**, *544*, 340.
- [47] Z. Zhao, Z. Fang, X. Han, S. Yang, C. Zhou, Y. Zeng, B. Zhang, W. Li, Z. Wang, Y. Zhang, J. Zhou, J. Zhou, Y. Ye, X. Hou, X. Zhao, S. Gao, Y. Hou, *Nat. Commun.* **2023**, *14*, 958.
- [48] K. S. Kim, D. Lee, C. S. Chang, S. Seo, Y. Hu, S. Cha, H. Kim, J. Shin, J. H. Lee, S. Lee, J. S. Kim, K. H. Kim, J. M. Suh, Y. Meng, B. I. Park, J. H. Lee, H. S. Park, H. S. Kum, M. H. Jo, G. Y. Yeom, K. Cho, J. H. Park, S. H. Bae, J. Kim, *Nature* **2023**, *614*, 88.
- [49] K. S. Kim, S. Seo, J. Kwon, D. Lee, C. Kim, J. E. Ryu, J. Kim, J. M. Suh, H. G. Jung, Y. Jo, J. C. Shin, M. K. Song, J. Feng, H. Ahn, S. Lee, K. Cho, J. Jeon, M. Seol, J. H. Park, S. W. Kim, J. Kim, *Nature* **2024**, *636*, 615.